Renewable Energy 76 (2015) 790–804

Contents lists available at ScienceDirect

Renewable Energy

journal homepage: www.elsevier.com/locate/renene

A hybrid methodology for the determination of the effective heat capacity of PCM enhanced building components

I.D. Mandilaras*, D.A. Kontogeorgos, M.A. Founti

National Technical University of Athens, School of Mechanical Engineering, Lab of Heterogeneous Mixtures and Combustion Systems, Heroon Polytechniou 9, 15780 Zografou, Greece

ARTICLE INFO

Article history:
Received 30 June 2014
Accepted 22 November 2014
Available online

Keywords:
PCM
Phase change materials
Numerical modeling
Heat flow meter apparatus
Effective heat capacity method
Differential scanning calorimetry

ABSTRACT

This paper presents a new hybrid methodology for the determination of the effective heat capacity (C_{eff}) of phase change materials (PCMs) for use in numerical models. The methodology focuses on PCM enhanced building panels utilizing a heat flow meter apparatus (HFMA) operating in dynamic mode and a numerical model based on the effective heat capacity method. It comprises of: a) experimental analysis of the panel by means of differential scanning calorimetry (DSC) and HFMA for the estimation of initial C_{eff} curves, b) optimization of the initial C_{eff} curves with an algorithm incorporating the numerical model and c) validation of the obtained results. Starting from a complete description of the concept and its main elements, the proposed approach has been successfully employed for the determination of C_{eff} curves of a lightweight building component combining insulation with thermal storage properties. The derived curves yielded more accurate results when incorporated in the numerical model than the respective curves measured by means of DSC. Simulations of the thermal performance of the building component in different conditions than those used for the determination of the curves validated the effectiveness of the methodology.

1. Introduction

Thermal mass enhancement of building components is of growing interest as the current construction practice shifts towards lightweight building shells. Due to their high latent heat density, phase change materials (PCMs) form an attractive solution that compensates for the small heat storage capacity of lightweight building components. Besides, the feasibility of incorporating PCMs in lightweight panels to increase their thermal inertia has already been demonstrated [1]. Moreover, the positive effect of the addition of PCM enhanced panels on the overall thermal performance of lightweight envelops has been experimentally verified [2]. Nevertheless, the development of a wall configuration incorporating PCMs requires extensive analysis in order to enable the researcher to deal with aspects regarding energy performance assessment and determination of the potential benefits. Therefore, modeling of latent heat storage in building components is essential for optimal design and material selection.

Numerical modeling of PCMs has been researched for several years and different approaches have been used [3]. Among them, the effective heat capacity method [4], which is widely used, is considered to be a versatile, convenient, adaptable and easily programmable method. The main advantage of this method is that the governing equations and the associated discretized equations have the general form of the heat conduction equation with a nonlinear heat capacity, namely the effective heat capacity (C_{eff}). As a result they can be solved with a standard heat transfer code. The key for accurate simulations lies in the appropriate selection of the nonlinear C_{eff} curves.

Up-to-date research cannot provide a satisfactory answer to the determination of C_{eff} curves appropriate for incorporation in PCM numerical models [5]. Literature in this field refers to two alternative practices. The first suggests the use of artificial C_{eff} curves based on the available properties of the PCM (e.g. phase change enthalpy, melting range etc.), while the other proposes the direct use of differential scanning calorimetry (DSC) thermographs. Regarding the artificial C_{eff} curves, the simplest approximation is the use of a step function, which has been proven to introduce large errors in the simulations [6]. The use of analytic functions can provide better results given that the parameters of these functions are appropriately selected [7] and [8]. Besides, the selection of these

* Corresponding author. Tel.: +30 6942993403.
E-mail address: gman@central.ntua.gr (I.D. Mandilaras).

http://dx.doi.org/10.1016/j.renene.2014.11.078
0960-1481/

parameters should refer to some kind of experimental work regarding the phase change characteristics of the simulated material. On the other hand, the direct incorporation of DSC thermographs in a numerical model is a widely accepted practice and appears to be a more reliable solution [9] and [10]. However, DSC measurements of the effective heat capacity of PCMs show a strong dependence on the heating rate, the sample mass and the direction of the temperature evolution (i.e. heating or cooling) [11] and [12]. Moreover, they require very small sample quantities (of the order of a few milligrams), so they may introduce significant errors when testing inhomogeneous materials with large-size representative volumes [13].

Such a problem can be partially overcome using the T-History method [14], an inexpensive and simple method for the determination of latent heat and melting range of PCMs. The improvements proposed by Kravvaritis et al. [15] can be utilized for the determination of C_{eff} as a function of temperature. In this method, the quantity of the sample is substantially bigger and can be representative of an inhomogeneous material. Nevertheless, despite the advantages of the T-history method, it cannot be implemented to measure the C_{eff} of large-scale envelope elements enhanced with PCM, such as gypsum boards or energy storage panels.

An alternative for the laboratory dynamic testing of PCM enhanced building materials and components is the heat flow meter apparatus (HFMA) operated in dynamic mode [16] and [17]. The main advantage of this device derives from the ability to measure test specimens of building materials in bulk form (e.g. concrete blocks) or in the form of boards (e.g. gypsum boards), thus overcoming the problems associated with the low quantity of the sample mass. Besides, for the same reason the concept of a dynamically operated HFMA (DHFMA) has already been used for the validation of numerical models simulating components incorporating PCMs [18].

In this study, a hybrid methodology combining DSC and DHFMA experiments along with an in-house developed simulation tool, named HETRAN [19], which was incorporated in an optimization routine, is proposed for the determination of the C_{eff} curves of PCM enhanced building panels. The proposed approach aims to overcome the shortcomings of the previously described practices in relation to the representativeness of the samples, by exploiting the ability of the HFMA to test PCM building panels in their final (ready to use) form. This paper describes and applies the proposed methodology on a lightweight envelope component consisting of a shape-stabilized PCM (SS – PCM) applied on the surface of an expanded polystyrene (EPS) insulation.

2. Methodology

This section provides a general description of the procedure and of the utilized experimental and numerical tools. DSC is omitted from the description of the main elements of the methodology, as it is a well established method for thermal analysis of PCMs [20] and [21].

2.1. General description

The flowchart shown in Fig. 1 summarizes the whole procedure of obtaining the C_{eff} curves of a PCM enhanced component. The methodology comprises four distinct steps:

- DSC and HFMA measurements
- Estimation of the initial C_{eff} curves
- Optimization of the C_{eff} curves
- Validation of the results

The procedure starts with testing a sample from the building component with a DSC. Measurements are performed with low heating rates in heating and cooling mode. From these measurements, a set of C_{eff} curves is defined. Throughout this paper, the term DSC C_{eff} will be used to refer to these curves. Higher heating rates are used for the estimation of the latent heat of fusion. Additional measurements, in the pure solid and liquid regions with blank curve correction and sapphire reference, define the specific heat capacity in solid and liquid state. Melting and solidification range and other thermal storage characteristics (e.g. melting temperature, solidification peaks etc.) can be studied in various heating

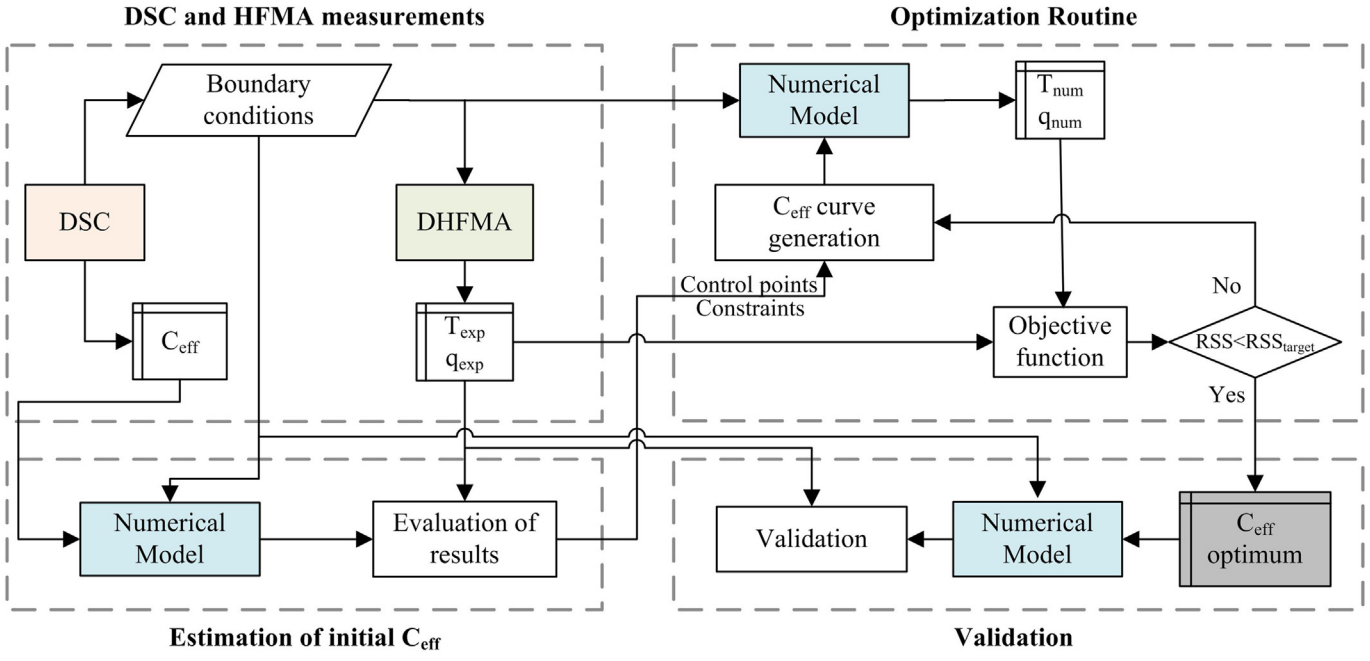

Fig. 1. Flowchart of the hybrid methodology.

rates in order to obtain a deeper understanding of the thermal storage behavior of the PCM.

The cyclic temperature boundary conditions for the DHFMA experiments are selected, using the melting and solidification range obtained from the DSC measurements. Taking into account that the C_{eff} curves will be used in order to simulate PCMs in building applications, the span of the cyclic temperature variations of the DHFMA should be in the range from 1 °C or 2 °C to 10–15 °C in a 24 h period. Temperatures and heat fluxes are measured at several locations inside the measured configuration. A minimum of two different sets of measurements is proposed: one for the optimization and one for the validation procedure.

In the next step, observations from the performed DHFMA experiments performed with the DHFMA and the DSC experiments are examined along with initial simulations using the DSC C_{eff} curves. Evaluation of the simulation results in comparison to the DHFMA results will suggest a proper choice for the shape of the artificial C_{eff} curves. From the suggested shape and a set of variables and constraints a large number of different artificial C_{eff} curves can be produced.

In the third step, the experimental results obtained from the DHFMA experiments and the initial artificial C_{eff} curves serve as input to the optimization procedure. The optimization algorithm generates different artificial C_{eff} curves according to the shape, variables and constraints of the previous step. Then, an iterative procedure takes place where the numerical model simulates the experimental test cases trying to define the C_{eff} curves that optimize the fit between the experimental results and the numerical simulations. The fitness is evaluated with standard statistical analysis. This analysis can be considered as an inverse curve fitting problem where the curve is defined by the experimental data (temperature or heat flow) and the algorithm searches for the set of the C_{eff} curves that when incorporated in the model achieve minimal differences between the target (experimental) and the numerical results. Thereby, the sum of the temperatures and/or heat fluxes residuals (*RSS*) at the measuring locations of the configuration serves as objective function for the optimization algorithm and is minimized as follows:

$$RSS_{temp} = \sum_{j=1}^{k} \sum_{i=1}^{n} \left(T^{j}_{num}(i) - T^{j}_{\exp}(i) \right)^2 \rightarrow \min. \quad (1)$$

and/or

$$RSS_q = \sum_{j=1}^{l} \sum_{i=1}^{n} \left(q^{j}_{num}(i) - q^{j}_{\exp}(i) \right)^2 \rightarrow \min. \quad (2)$$

where index n stands for the total time steps of the simulation, while k and l are the numbers of measuring locations of temperature and heat flux, respectively.

Finally, in order to verify the proposed optimum artificial curves and assess the limits of their applicability, additional numerical simulation results are compared to experimental data sets obtained by altering the initially used boundary conditions or the measuring configuration.

2.2. The dynamic operated heat flow meter apparatus (DHFMA)

The DHFMA used for the cycle temperature measurements of the PCM component is designed and constructed according to the general guidelines provided by international standards describing the heat flow meter apparatus (HFMA) [22] and [23]. When operated in constant temperature boundary condition it constitutes a typical HFMA, capable of measuring thermal conductivity of flat slab specimens. The dynamic operation oriented design of the temperature control and data acquisition system facilitates the operation of the setup in dynamic mode in line to the recently introduced ASTM C1784-13 standard [24]. This standard applies in the measurement of thermal storage properties of PCMs using an HFMA. It covers the measurement of non-steady state heat flow into or out of flat slab specimens and thus, addresses the needs of cyclic temperature measurements as well. Therefore, recommendations given by this standard are largely followed in this study and adjusted according to the requirements of the cyclic temperature boundary conditions.

The setup of the DHFMA is schematically depicted in Fig. 2. It includes a sample holder with two heating/cooling plates, two thermoelectric devices, a cooling unit with a storage tank, a primary and a secondary water circuit, a control unit, several temperature and heat flux sensors, a data acquisition device and a PC with the appropriate software. The core of the device is the sample holder assembly, comprising of two heating/cooling plates, each one mounted vertically on a support frame. A rail system allows the displacement of the plates to adjust to the thickness of the specimen.

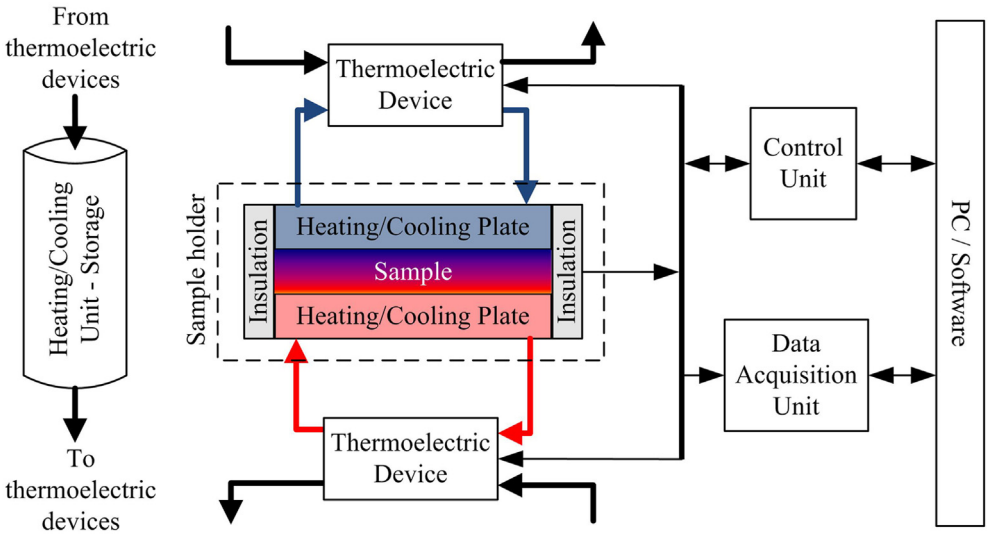

Fig. 2. Schematic diagram of the DHFMA setup.

During operation, the control unit regulates the temperature on the working surfaces of the plates according to the user defined temperature profile assigned to each plate. Temperature regulation is achieved with water circulation from the thermoelectric devices to the plates of the sample holder. The temperatures and heat fluxes are recorded on the plates and at several locations of the specimen.

Before each set of measurements the temperature sensors are calibrated in a dry well calibrator that ensures an accuracy of ca. ±0.05 °C. Their fine measuring tip (<0.5 mm) allows accurate positioning inside the measuring configuration. Heat flux sensors are calibrated according to ISO 8301 and ASTM C518 for multiple temperature points, providing uncertainty values between ±0.15 W m^{-2} (for heat flux values near 0 W m^{-2}) and ±0.50 W m^{-2} (for heat flux values near 15 W m^{-2}). However, the calibration protocol described in ISO 8301 and ASTM C518 stands for steady state measurements. Heat storage effects in the heat flux sensors, associated with the dynamic nature of the measurements, as described in annex 1 of ASTM C1784-13 [24], can further increase this error by ca. 0.11 W m^{-2}. This is mainly expected for the relatively high heating rates, observed (in the measurements of this study) during low heat flux values.

It should be noted that all the above mentioned standards refer to certain experimental protocols that differ from the procedure followed in this study. Even in ASTM C1784-13, where dynamic operation conditions are considered, the sample is tested under a series of small temperature steps applied on both plates. On the other hand, in this study the temperature of the one plate is held constant while the temperature of the other varies sinusoidally with amplitude up to 15 °C. As a result, the calibration factors of the heat flux sensors may slightly differ from the ones calculated under steady state conditions and constant temperature difference between the two plates (according to ISO 8301 and ASTM C518 standards). Thus, the uncertainty of heat flux measurements may slightly further increase.

2.3. The numerical model

A general purpose one-dimensional heat transfer code is utilized for all the simulations required in the proposed methodology. The in-house developed HETRAN code has been described and validated in previous works published by the authors [19,25] and [26]. It employs the general form of the transport equation (Eq. (3)) including terms for storage, convection diffusion and generation and thus, it is appropriate for simulating heat and moisture transfer inside multilayer porous building materials without fluid flow.

$$A_f\frac{\partial f}{\partial t} = \nabla\left(B_f\nabla f\right) - \nabla\left(C_f f\right) + Q_f \tag{3}$$

By omitting the terms for diffusion and generation ($C_f = 0$ and $Q_f = 0$) the conductive heat transfer equation is derived.

$$\rho C\frac{\partial T}{\partial t} = \frac{\partial}{\partial x}\left(k\frac{\partial T}{\partial x}\right) \tag{4}$$

On the other hand the conserved formulation of the Stefan problem [27] reads:

$$\rho\frac{\partial h}{\partial t} = \frac{\partial}{\partial x}\left(k\frac{\partial T}{\partial x}\right) \tag{5}$$

By applying the chain rule of differentials (Eq. (6)), Eq. (5) is modified to the effective heat capacity method equation (Eq. (7)).

$$\frac{\partial h}{\partial t} = \frac{\partial h}{\partial T}\frac{\partial T}{\partial t} = C_{eff}\frac{\partial T}{\partial t} \tag{6}$$

$$\rho C_{eff}\frac{\partial T}{\partial t} = \frac{\partial}{\partial x}\left(k\frac{\partial T}{\partial x}\right) \tag{7}$$

From Eqs. (4) and (7) it becomes clear that the code can provide accurate solution to the phase change problem as long as the effective heat capacity term C_{eff} is properly defined. It is noted that in the above equations and throughout this paper the term effective heat capacity refers to the intensive form of the quantity (i.e. specific heat capacity measured in J·kg^{-1}·K^{-1}).

Regarding the numerical solution of Eq. (7), HETRAN uses the DIVPAG routine from the International Mathematics and Statistics Library (IMSL) [28]. DIVPAG solves initial value problems using Gear's backward differentiation formula (BDF) method with automatic control of step size and order [29]. The temporal scheme is fully implicit.

3. Implementation of the proposed approach on a PCM – EPS component

The methodology presented so far has been implemented in order to determine the effective heat capacity of a shape-stabilized PCM (SS – PCM) applied on the surface of an EPS insulation. After the analysis of thermal storage properties of the PCM with DSC measurements, the component is tested in a DHFMA. Two different test cases are examined. The results from the first are utilized in the optimization algorithm for the determination of optimum C_{eff} curves. The second test case is used for validation purposes.

3.1. Materials

A ca. 5 mm thick layer of the SS – PCM is uniformly applied on the one side of a ca. 30 mm EPS (EPS type I) panel resulting to a component that can be added in lightweight wall configurations to enhance insulation and thermal mass of the structure. An additional thin layer of EPS (EPS type II) is used as an interface material between the SS – PCM and the plates of the DHFMA during the measurements. The reason for the use of this additional layer is explained in section 3.3. The area of the tested specimens is 200 × 200 m^2. The properties of the materials are presented in Table 1.

3.2. Differential scanning calorimetry analysis

The Mettler Toledo DSC 1 Star^e system is deployed in order to measure the thermal storage properties of the PCM. The module is fitted with the FRS5 sensor. The measuring principle is based on the well proven Boersma principle [30] (fixed thermocouple differential thermal analyzer) in which the temperature difference between

Table 1
Thickness and thermophysical properties of the materials.

Material	Thickness [mm]	Apparent density [kg m^{-3}]	Specific heat capacity [J kg^{-1} K^{-1}]	Thermal conductivity [W m^{-1} K^{-1}]
EPS type I	31.4[a]	31[a]	1450[b]	0.032[a] (10 °C) 0.033[a] (20 °C) 0.034[a] (30 °C)
EPS type II	5.7[a]	19[a]	1450[b]	0.034[a] (10 °C) 0.035[a] (20 °C) 0.036[a] (30 °C)
SS – PCM	4.8[a]	792[a]	2600[a] solid 2200[a] liquid	0.182[a] solid 0.141[a] liquid

[a] Measured values.
[b] Values provided by the producer.

a sample and a reference material is measured and the heat flow is calculated by calibration data. The properties addressed in terms of DSC include the estimation of the DSC C_{eff} curves, the determination of the specific heat capacity in solid and liquid state, the estimation of phase change enthalpy and the determination of melting and crystallization range.

3.2.1. General observations

Measurements are performed at four different heating/cooling rates (Fig. 3). Heating of the sample at 10 °C min^{-1} (Fig. 3a) reveals three levels of constant heat capacity. The first is below −25 °C, the second is between −13 °C and −8 °C and the third is above 55 °C. The variation from the first to the second level is associated with the glass transition of the polymer supporting material. The stabilized heat capacity observed in the region between −13 °C and −8 °C corresponds to the SS − PCM panel (in its flexible form) with the PCM in the solid state. In the temperature region above 55 °C the heat capacity stabilizes in the value that corresponds to the SS − PCM panel with the PCM in the liquid state. A dominant melting peak at ca. 22 °C is followed by a secondary peak near

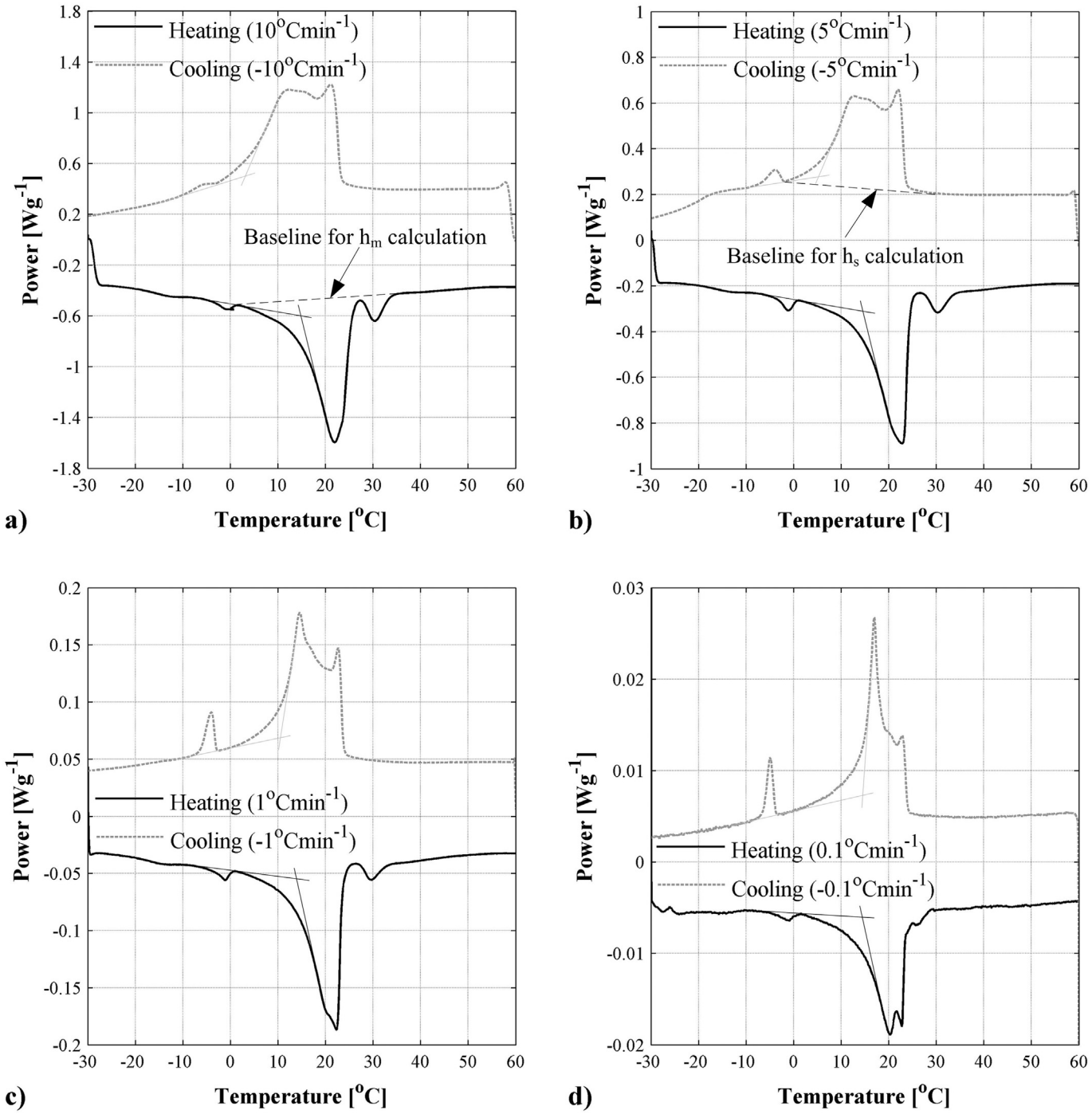

Fig. 3. DSC measurements of the SS − PCM at four different heating/cooling rates: (a) 10 °C min^{-1}, (b) 5 °C min^{-1}, (c) 1 °C min^{-1} and (d) 0.1 °C min^{-1}.

30 °C. In cooling mode this secondary peak at 30 °C disappears and solidification starts at approximately 23 °C. The solidification range appears to be wider than the respective melting range. The same behavior with minor changes is also observed in the heating/cooling rates of 5 °C min^{-1} (Fig. 3b).

As the cooling rate decreases to 1 °C min^{-1} (Fig. 3c), the solidification enthalpy is shifted towards lower temperatures and a peak near 14 °C is observed. This peak grows further at the lower cooling rate of 0.1 °C min^{-1} (Fig. 3d) and appears to move towards higher temperatures (near 17 °C). In the heating mode a marked change is observed only at the lowest heating rate (Fig. 3d), where the melting peak splits to form a second peak of approximately the same height. In addition, the low melting peak appearing at 30 °C for higher heating rates, shifts towards lower temperatures and tends to merge with the dominant melting peak.

3.2.2. Melting/solidification range

The characteristic temperatures of all the thermographs are summarized in Table 2. Melting onset and solidification endset are estimated by the section of appropriate lines shown in Fig. 3. As expected, lower heating/cooling rates result in lower melting endset and higher solidification onset (lower subcooling degree), respectively. Besides, in line with the literature [31], for lower cooling rates solidification enthalpy is distributed in a smaller range. Melting and solidification range (endset minus onset temperature) appear to converge to the same value (ca. 10 °C) at the low heating rate of 0.1 °C min^{-1}. On the other hand, melting enthalpy is more evenly distributed in this range than the respective solidification enthalpy, which is mainly concentrated under the dominant solidification peak.

3.2.3. Specific heat capacity

The determination of the specific heat capacity of the materials is standardized in ISO 11357-4:2005 [32] and ASTM E1269-11 [33]. According to both standards, measurement is possible only to thermally stable solids and liquids. This means that apart from sensible heating other overlapping thermal events must not occur during the DSC measuring procedure. Therefore, in order to assign values of constant heat capacity for the solid and liquid phase of the SS – PCM panel only the temperature regions outside the melting range and other phase transformations (such as glass transitions) of the material are considered. The temperature interval between −13 °C and −10 °C is used for the solid – state heat capacity (C_s) and the region above 55 °C for the liquid – state heat capacity (C_l) determination. The measurements involve heating of an empty crucible of a reference material and of the SS – PCM sample at a controlled rate in a controlled atmosphere through the temperature region of interest. A heating rate of 10 °C min^{-1} is used.

The reference sample consists of two synthetic sapphire disks (4.8 mm diameter and 24 mg each). The mass of the SS – PCM samples is approximately 15 mg, in order to provide heat capacity that matches the heat capacity of the sapphire standard and at the same time to provide a heat flow signal between 5 and 10 mW.

Table 2
Characteristic temperatures of heating and cooling DSC thermographs.

Heating rate	Melting			Solidification		
[°C min^{-1}]	Onset [°C]	Main peak [°C]	Endset [°C]	Onset [°C]	Main peak [°C]	Endset [°C]
10	15.0	21.9	34.7	23.3	21.1	3.5
5	13.8	22.9	34.2	23.6	22.0	5.6
1	13.7	22.3	33.3	23.9	14.5	10.6
0.1	14.3	20.3	29.1	24.8	17.0	14.3

Table 3
Results of the individual measurements and mean values of the specific heat capacity of the SS – PCM in solid and liquid state.

	C_s [J kg^{-1} K^{-1}]			C_l [J kg^{-1} K^{-1}]		
	1st scan	2nd scan	3rd scan	1st scan	2nd scan	3rd scan
1st set	2570	2596	2575	2224	2202	2173
2nd set	2606	2640	2636	2215	2195	2201
Mean value	2604 ± 32			2201 ± 27		

Since small quantities of specimen are used, the measurements are duplicated with a different sample, in order to assure homogeneity and representativeness. Each sample is measured three times for accuracy improvement.

Taking all possible error sources into account, the total measurement error of a single specific heat measurement is estimated equal to ±3%. Table 3 shows the values of the specific heat capacity obtained from the two measurement sets (corresponding to the two different samples) for the solid and liquid material.

3.2.4. Phase change enthalpy

Enthalpy of melting (h_m) and solidification (h_s) is determined by the standard method described in ASTM E793-06(2012) [34] and ISO 11357-3:2011 [35]. Following the guidelines of these standards, a sample of approximately 8 mg is cooled down to −30 °C and held for 2 min. Afterwards, the specimen is heated using a 10 °C min^{-1} heating rate through the melting range until the baseline is reestablished at 55 °C. The specimen is held at this temperature for 2 min and then is cooled down to −30 °C. A cooling rate of 5 °C min^{-1} is used, as the cooling capability of the available chiller does not allow a cooling rate as high as 10 °C min^{-1} for temperatures lower than 0 °C. Solidification and melting enthalpies are quantitatively estimated by using a linear approximation for the baselines above and below melting and solidification regions, respectively. The energy under the peak located below 0 °C is not included in the calculations (this study concerns temperatures well above 0 °C). The temperature ranges and the respective baselines used for the calculation of melting and solidification enthalpies are shown in Fig. 3a and b. For accuracy improvement the measurements are repeated two more times. The mean value of the solidification enthalpy is 66.3 kJ kg^{-1} in the temperature range between −3 °C and 30 °C, while the mean value of the melting enthalpy amounts to 64.1 kJ kg^{-1} in the range of 2 °C to 35 °C (Table 4).

3.2.5. Effective heat capacity by DSC

As already mentioned, the estimation of the C_{eff} curves by means of DSC, is not standardized. Nevertheless, literature suggests the use of heating rates as low as 0.1 °C min^{-1} [20] [36], and [37]. In this study, the DSC C_{eff} curves are derived from the measurements at 0.1 °C min^{-1} presented in Fig. 3d. The used heating rate is not the lower limit of the currently used DSC equipment, but a compromise to take into account the consequences of signal-to-noise ratio. For heating rates lower than the selected one, the signal-to-noise ratio

Table 4
Results of the individual measurements and mean values of the melting and solidification specific phase change enthalpies.

	h_s [kJ kg^{-1}]			h_m [kJ kg^{-1}]		
	1st scan	2nd scan	3rd scan	1st scan	2nd scan	3rd scan
1st set	64.9	65.2	67.5	64.5	63.1	65.6
2nd set	67.8	66.9	65.5	63.8	62.9	64.9
Mean value	66.3 ± 0.8			64.1 ± 0.8		

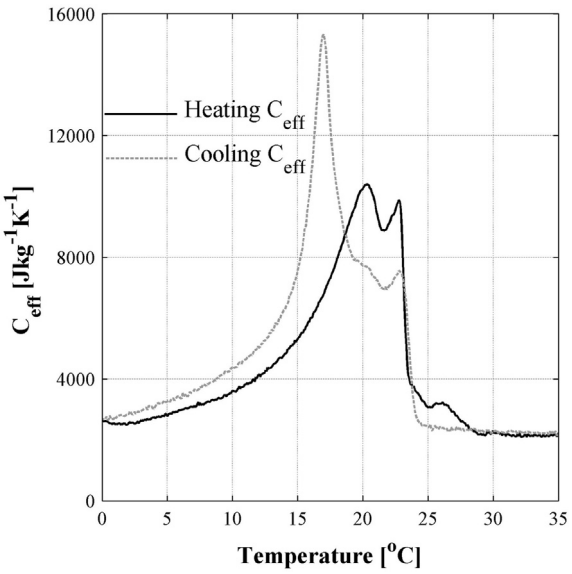

Fig. 4. Effective heat capacity curves for heating and cooling processes obtained by DSC measurements at 0.1 °C min^{-1}.

increases significantly and the error introduced in the measurements is considerable. Besides, this is one of the main limitations in the use of the DSC in dynamic mode for calorimetry of PCMs [11].

In order to calculate the effective heat capacity, the normalized DSC measured power (in W g^{-1}) is divided by the heating rate (in °C s^{-1}) resulting in the curves shown in Fig. 4. The fact that the phase change energy in the melting process is concentrated in a higher temperature region than in the cooling process reveals a light hysteresis of the material, which is generally in-line with the literature for paraffin based PCMs [38,39] and [40].

DSC measurements in low heating rates cannot provide adequate accuracy for absolute values of heat capacity [34], thus the baseline of both curves is shifted so that the stabilized value above 30 °C matches the measured value for the SS – PCM with the PCM in the liquid phase (2200 J kg^{-1} K^{-1}). Integration of the curves in the temperature range of melting and solidification is equal to the melting (67.3 kJ kg^{-1}) and solidification enthalpies (68.1 kJ kg^{-1}). The values deviate slightly from the respective values determined with the standardized procedure in section 3.2.4.

3.3. DHFMA measurements

According to the results of the DSC experiments, the prototype PCM – EPS component is tested with the DHFMA in temperature profiles ranging from 10 °C to 25 °C. Since the phase change behavior of PCMs depends on the temperature and the heating rate of the application, the tests for this research have been performed using realistic boundary conditions. The tested component is treated as an envelope element exposed to indoor and outdoor temperature conditions. Defining and validating the C_{eff} curves in such conditions ensures that they are appropriate for use in numerical modeling of building envelopes.

Since the DHFMA cannot provide convective boundary conditions, a thin insulation interface (EPS Type II) is introduced between the heating/cooling plate of the device and the surface of the SS – PCM, in order to simulate the convection conditions on the exposed side of SS – PCM. The thickness of the insulation is set to 5.7 mm corresponding to a convection coefficient value of approximately 6 W m^{-2} K^{-1}. This value applies for wind speeds ranging between −1 m s^{-1} and −4 m s^{-1} [41]. For the convection boundary condition on the other side of the configuration the first 5.4 mm of the existing EPS panel are assumed to serve as an interface between the plate surface and the rest of the component corresponding to a convection coefficient value equal to approximately 6 W m^{-2} K^{-1}. This means that the studied configuration corresponds to a test case consisting of 5 mm SS PCM panel connected with a 26 mm EPS exposed in air on both sides.

In the DHFMA configuration, the surface of the component treated with the SS – PCM is assumed to be exposed to outdoor daily temperature variation approximated by a sinusoidal temperature profile. A constant temperature is assigned to the other heating/cooling plate simulating indoor conditions. Temperature and heat flux is measured at several locations in the configuration as shown in Fig. 5.

Two different test cases, relating to different boundary conditions, were studied (Fig. 6). In the first case ('test case 1'), the indoor temperature is set equal to 20 °C, close to the melting peak near the center of the PCM active range. Outdoor temperature varies from 15 °C to 25 °C, covering almost the entire phase change range. In the second case ('test case2'), the indoor temperature is kept at 17,5 °C lying close to the solidification peak of the PCM (Fig. 3d) and outdoor diurnal temperature range is wider by 5 °C than the first case reaching a lowest temperature of 10 °C. The initial temperature of both test cases is equal to the indoor stable temperature.

3.4. Estimation of initial artificial C_{eff} curves

The DHFMA measurements of 'test case 1' are initially simulated with the use of the DSC C_{eff} curves. The numerical model uses either the heating or the cooling C_{eff} curve depending on the direction of the process. It also takes into account the thermal conductivity of the materials as a function of temperature (Table 1). Particularly for

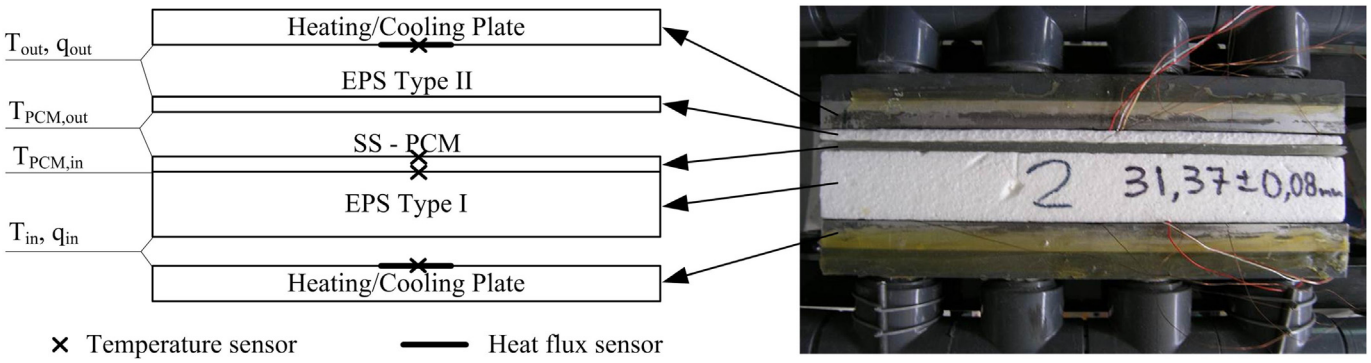

Fig. 5. Schematic diagram and photograph of the DHFMA showing the location of temperature and heat flux sensors.

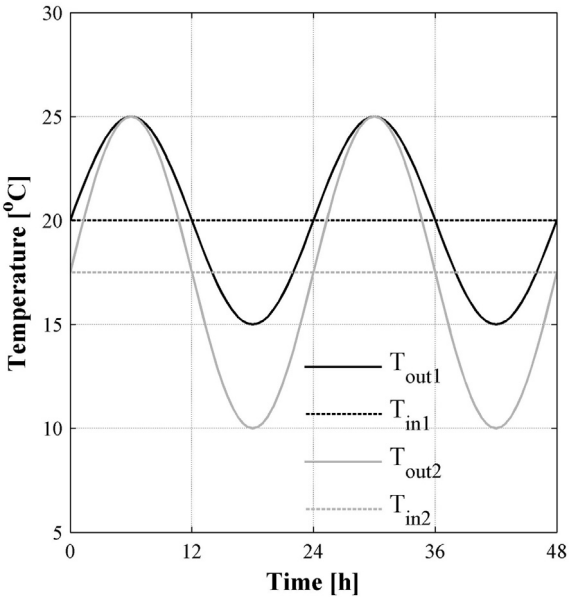

Fig. 6. Temperatures imposed on the two sides of the PCM – EPS component by the Dynamic operated Heat Flow Meter Apparatus.

the SS-PCM where the values for solid and liquid PCM are known, a linear approximation is used to calculate the thermal conductivity as a function of liquid to solid ratio (liquid fraction). Then, with the use of the C_{eff} curves (from which the liquid fraction versus temperature can be easily derived) the thermal conductivity versus temperature inside the phase change range is defined. The density of all the materials is assumed to be constant. The predictions of the temperature and heat flux evolution at the measurement locations are compared with the respective experimental data, as shown in Fig. 7.

The most noticeable difference between the experimental and the numerical temperature evolution on both sides of the SS – PCM (Fig. 7a and b) appears during cooling process near 19,5 °C. The intense solidification region that is indicated by temperature stabilization cannot be captured by the simulations. This can be clearly seen in Fig. 8a where the temperature curves near the region of 19.5 °C are shown. The discrepancy is related to the solidification peak in the DSC cooling C_{eff} curve (Fig. 4). Firstly, the temperature of the peak is approximately 2 °C lower than the solidification temperature during the DHFMA measurements. Secondly, the area under the peak that represents the phase change enthalpy during the intense solidification region appears to be low and is unable to reproduce a stabilized temperature.

Further inconsistencies of temperature evolution can be observed in the minimum and maximum temperatures of the cycle and the rate of temperature increase and decrease. The simulated temperature evolution rate is slightly higher than the experimental one, resulting to higher maximum and lower minimum temperatures. This can be attributed to a relatively low thermal mass assigned to the PCM in the temperature range of the cycling variation. Given that the total phase change enthalpy is accurately measured, the low thermal mass can only be the result of a wider phase change range.

In line with the above comments, there are two major discrepancies in the heat flux evolution. The first is the heat flux stabilization near zero levels during the cooling process at the interface between SS – PCM and EPS (Fig. 7d). A more detailed view of this region is shown in Fig. 8b. The second is the maximum and minimum heat flux values at the surface of the SS – PCM exposed to the cycling temperature variation (Fig. 7c). As in the case of the temperature evolution, the first issue is associated with the solidification peak, while the second is associated with the temperature range of the phase change during melting and solidification obtained by the DSC measurements.

According to the suggested methodology and based on the above observations and the DSC C_{eff} curves, a general shape is assigned to an artificial heating and cooling C_{eff} curve (Fig. 9). The previously discussed deviations between the experimental results and the predictions (using the DSC C_{eff} curves) indicate an appropriate number of control points that define the shape of the artificial C_{eff} curves. The control points of the curves are shown in Fig. 9. The arrows in the same figure denote whether the temperature and/or C_{eff} value of a control point is an optimization variable (ranging between appropriate values) or it is restricted (fixed or calculated value). The area below both curves corresponds to the total phase change enthalpy and it is constrained to the measured value of 65.2 kJ kg^{-1} (i.e. the mean value of the measured melting and solidification enthalpies). Eqs. (8) and (9) are the restrictions derived by setting the calculated area equal to the measured value of the phase change enthalpy for cooling and heating respectively:

$$-(\Delta T_{61}+\Delta T_{52})C_1+\Delta T_{64}C_2+\Delta T_{31}C_3+\Delta T_{53}C_4+\Delta T_{42}C_5=65.2\cdot 2 \tag{8}$$

$$C_2=C_1+2\cdot 65.2/(\Delta T_{41}+\Delta T_{32}) \tag{9}$$

where ΔT_{ij} stands for the difference $T_j - T_i$.

Table 5 presents in detail the constraints of the control points of cooling and heating curves respectively. The specific heat capacity of control point 4 of the cooling curve is calculated by Eq. (8) whereas the specific heat capacity of control point 2 of the heating curve is calculated by Eq. (9). The specific heat of SS – PCM in the solid and liquid state is considered constant and equal to that of the liquid phase (2200 J kg^{-1}). This is suggested by the DSC curves at the heating rate of 0.1 °C·min^{-1} showing the same specific heat capacity value before and after the phase change process. This assumption is discussed in paragraph 3.6.

3.5. Optimization procedure

The strategy used in this study was to begin optimization with a course grid within the range of possible values of each variable and then refine the grid near the values appearing to minimize the RSS. This resulted to approximately 4000 different pairs of heating and cooling curves requiring a total computational time of approximately 70 h in order to obtain the final curves. The minimization of the temperature RSS (Eq. (1)) was selected as optimization criterion. Extensive calibration and accurate positioning of temperature sensors took place in order to ensure the accuracy of the results. On the other hand, as already explained in paragraph 2.2, the calibration procedure for the heat flux sensors is based on steady state measurements and thus cannot assure the same levels of accuracy.

The experimental results of test case 1 and the corresponding boundary conditions are utilized for the procedure. Tables 6 and 7 tabulate the optimized values of the control points for the cooling and heating curves, respectively.

The optimized cooling artificial C_{eff} curve (Fig. 10a) follows the trend of the cooling DSC C_{eff} curve with three major differences regarding the dominant peak, the solidification onset and the separation of the two peaks of the curve. The dominant peak is

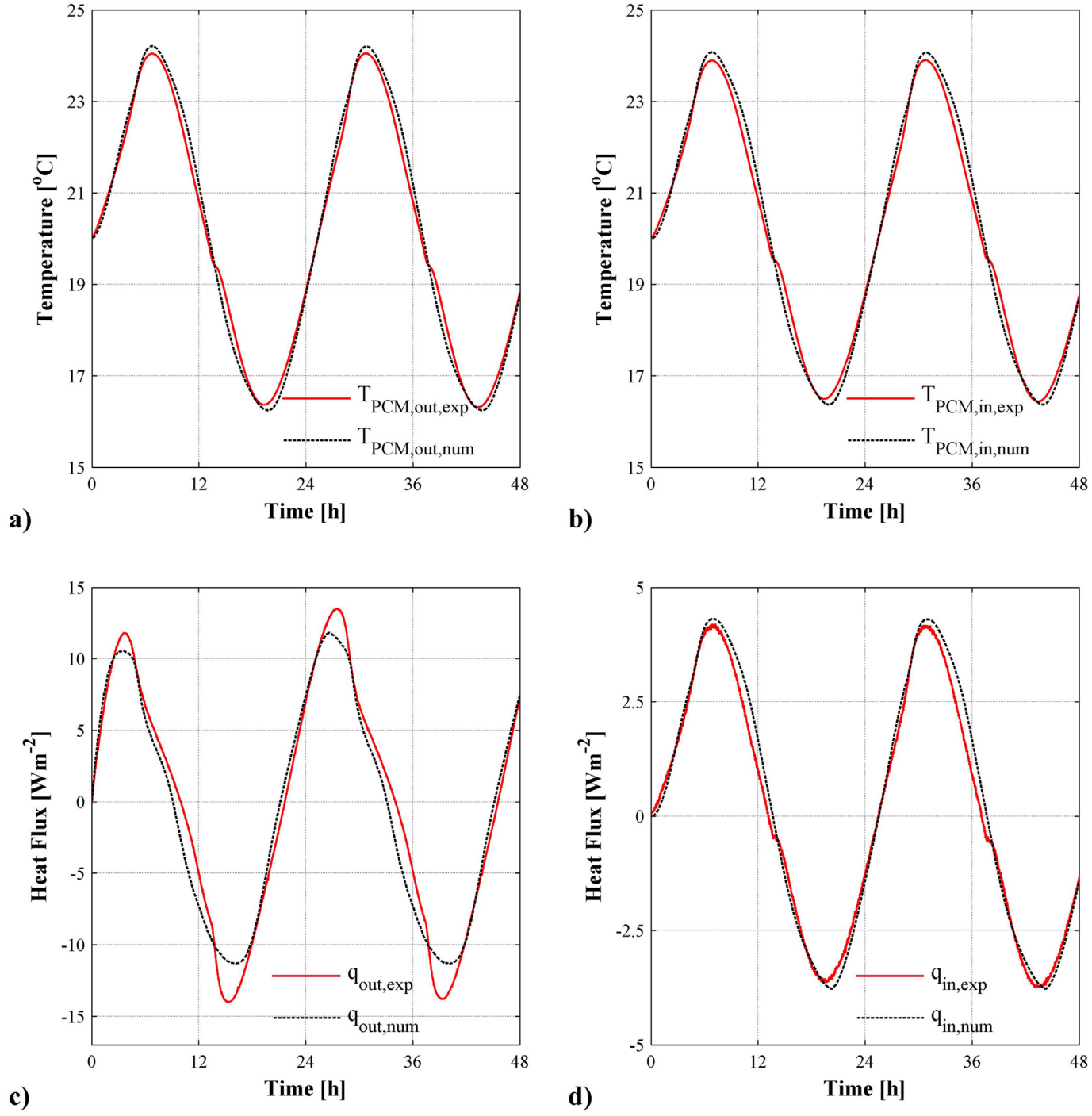

Fig. 7. Comparison between the experimental data and the predictions using the DSC C_{eff} curves of (a) temperature at the exposed side of the SS − PCM, (b) temperature at the interface of SS − PCM and EPS, (c) heat flux at the heating/cooling plate simulating outdoor conditions and (d) heat flux at the heating/cooling plate simulating indoor constant temperature.

shifted towards higher temperatures, while its maximum value is elevated at very high levels. Moreover, the span of the peak is also very narrow ($\Delta T = 0.1$ °C) in comparison to the respective DSC span. The onset of the solidification reaction is 2 °C lower compared to the DSC results indicating a more intense subcooling effect in the DHFMA measurements. Finally, a clear separation is observed in the two peaks of the curve.

In case of the heating C_{eff} curve (Fig. 10b), the absence of subcooling results to an optimized curve similar to the DSC curve. The range of the curve is narrower than the respective DSC curve. It is noted that the optimized curve does not take into account the two distinctive peaks of the DSC curve. Within the framework of this study, the introduction of two distinctive peaks in the curve was not considered necessary as it would compromise the

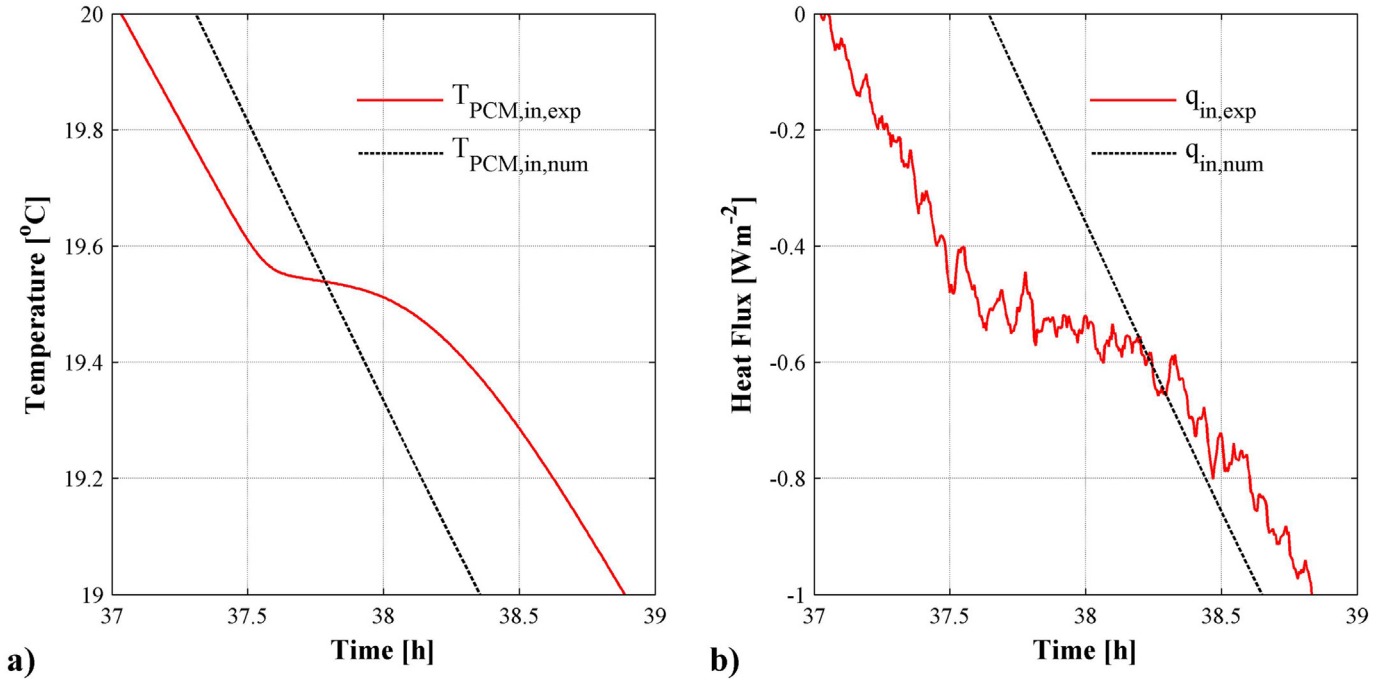

Fig. 8. Comparison between the experimental data and the predictions using the DSC C_{eff} curves. (a) Detailed view of Fig. 7a and (b) Detailed view of Fig. 7d.

computational time. The error introduced by the omission of a second curve is discussed in paragraph 3.6.

Predictions of test case 1 using the optimized curves (Fig. 11) are obviously improved in comparison to the respective numerical results produced using the DSC derived curves. The deviations between the predictions and the experimental results are negligible. Minimum and maximum predicted temperature and heat flux values are very close to the respective experimental values and the rates of the temperature increase/decrease have been reduced. Finally, the temperature and heat flux stabilization during the solidification process is now accurately predicted in the simulations (Fig. 12).

It should be noted that the relatively high uncertainty assumed for the heat flux measurements does not affect the above analysis for several reasons. Firstly, the comparison of the experimental and simulated temperature evolution can, alone, provide strong

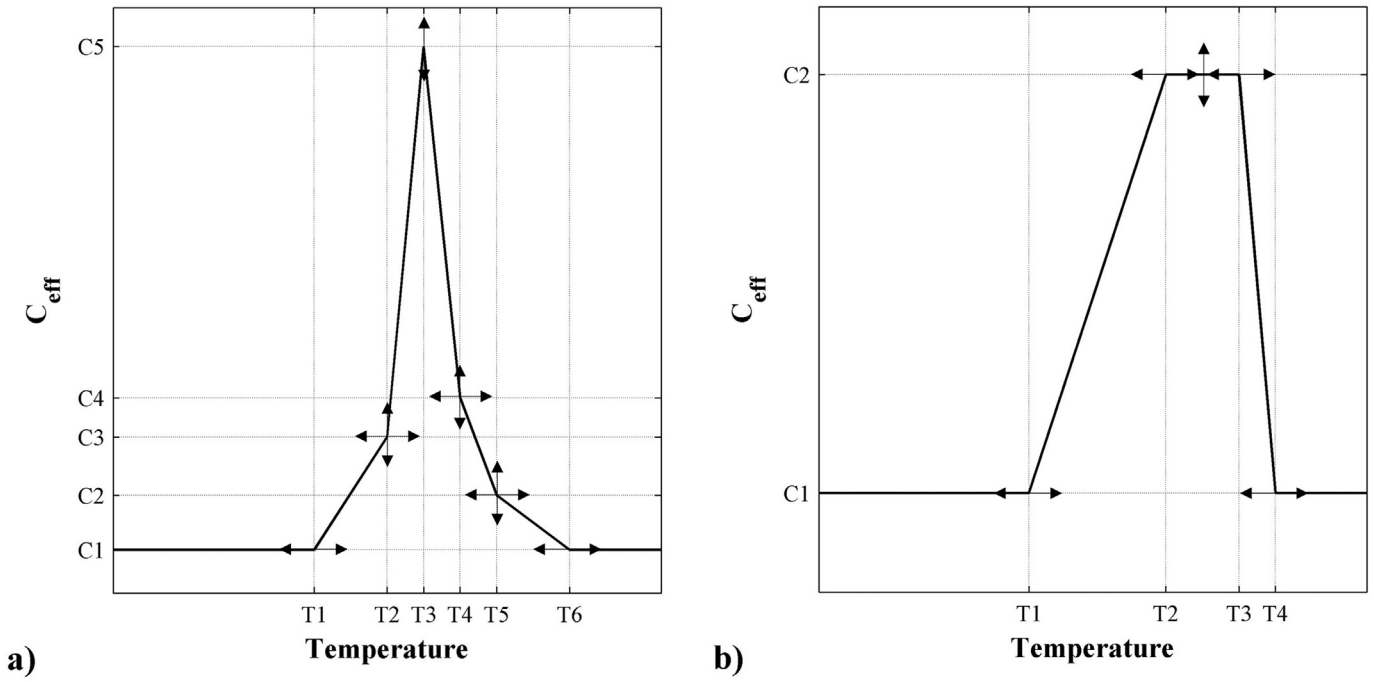

Fig. 9. Shape and variables of the initial artificial a) cooling and b) heating C_{eff} curves.

Table 5
Constraints of the control points of the cooling and heating curves.

Variable	Cooling curve			Heating curve		
	Range ([°C] or [J kg^{-1} K^{-1}])	Value ([°C] or [J kg^{-1} K^{-1}])	Degree of freedom	Range ([°C] or [J kg^{-1} K^{-1}])	Value ([°C] or [J kg^{-1} K^{-1}])	Degree of freedom
T_1	10–15	–	Range	10–14.5	–	Range
T_2	19–20	–	Range	16–22	–	Range
T_3	19–20	–	Range	21–25	–	Range
T_4	19–20	–	Range	22–26	–	Range
T_5	19–25	–	Range	–	–	–
T_6	21–25	–	Range	–	–	–
C_1	–	2200	Fixed	2200	–	Fixed
C_2	2200–30,000	–	Range	–	Equation (9)	Calculated
C_3	30,000–100,000	–	Range	–	$C_3 = C_2$	Calculated
C_4	–	Equation (8)	Calculated	2200	–	Fixed
C_5	2200–30,000	–	Range	–	–	–
C_6	–	2200	Fixed	–	–	–

Table 6
Optimized values of the control points for the cooling curve.

Variables	Control point					
	1	2	3	4	5	6
T [°C]	11.15	19.45	19.50	19.55	20.05	22.25
C_{eff} [J kg^{-1} K^{-1}]	2200	14,770	88,320	1870	8200	2200

Table 7
Optimized values of the control points for the heating curve.

Variables	Control point			
	1	2	3	4
T [°C]	11.55	21.50	21.85	24.90
C_{eff} [J kg^{-1} K^{-1}]	2200	11,490	11,490	2200

evidence for the quality of the C_{eff} curves used in the model. Heat flux measurements support and verify these results. Secondly, apart from the quantitative nature of the comparisons related to the accuracy of the measurements, the trend of the simulated curves is obviously improved with the use of the optimized C_{eff} curves.

3.6. Validation of the optimized curves

Since the artificial C_{eff} curves were calibrated in order to produce accurate results for a given configuration and boundary conditions, a different test case is needed in order to ensure the validity of the curves. Thus, 'test case 2' (outdoor temperature in the range of 10 °C–25 °C) is simulated with the use of the optimized curves and the results are compared with the experimental data obtained by the DHFMA measurements (Fig. 13).

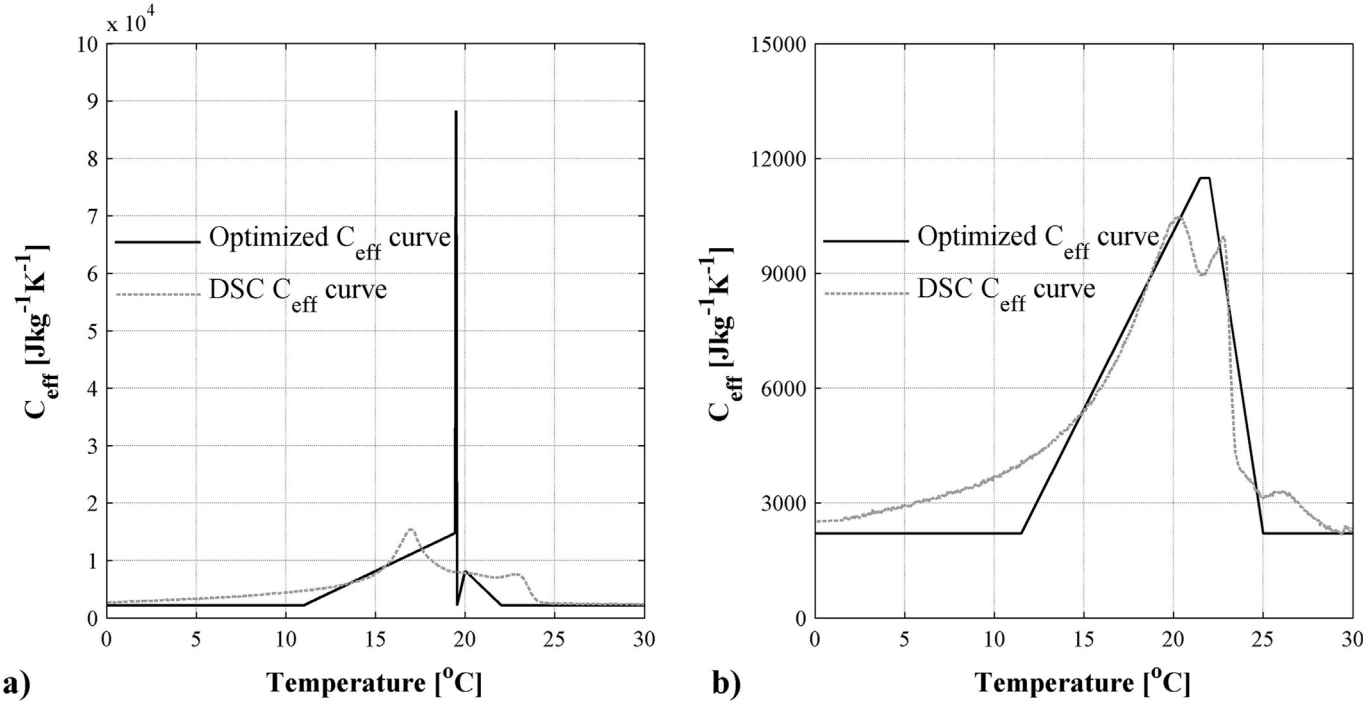

Fig. 10. Optimized artificial C_{eff} curves of the SS – PCM in comparison with the respective DSC curves for (a) cooling process and (b) heating process.

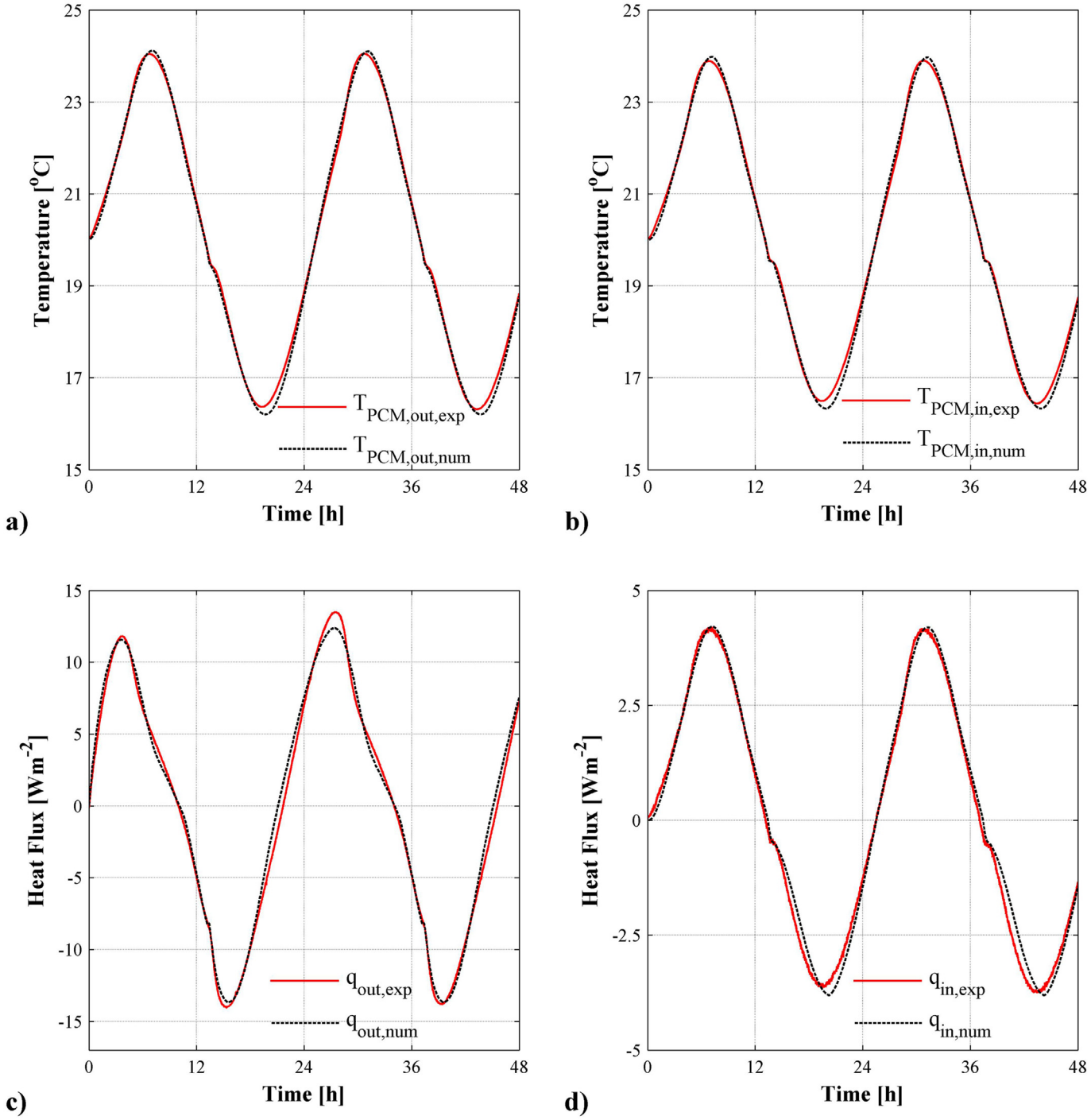

Fig. 11. Comparison of the experimental with the predicted values using the optimized artificial C_{eff} curves of (a) temperature at the exposed side of the SS – PCM, (b) temperature at the interface of SS – PCM and EPS, (c) heat flux at the heating/cooling plate simulating outdoor conditions and (d) heat flux at the heating/cooling plate simulating indoor constant temperature.

Temperature evolution (Fig. 13a and b) shows good agreement with the experimental curves with a small under-prediction of the minimum temperatures. This discrepancy is probably associated with the specific heat of the SS – PCM in solid state. This was assumed constant and equal to the specific heat of the SS – PCM in liquid state according to DSC measurements at 0.1 °C min^{-1}. It appears that the use of a higher heat capacity for the PCM in the solid state would be more appropriate. DSC measurements of the constant heat capacity at −10 °C provided a value of 2600 J kg^{-1} K^{-1}. An interpolation between the solid (2600 J kg^{-1} K^{-1}) and liquid (2200 J kg^{-1} K^{-1}) value at the temperature where the constant C_{eff} is assigned to the solid PCM (ca. 11 °C) would suggest a value of 2370 J kg^{-1} K^{-1} instead of 2200 J kg^{-1} K^{-1}. This reveals another aspect of the issues arising from the estimation of the effective capacity at very low heating rates. It is most probably that the resulting low levels of the DSC

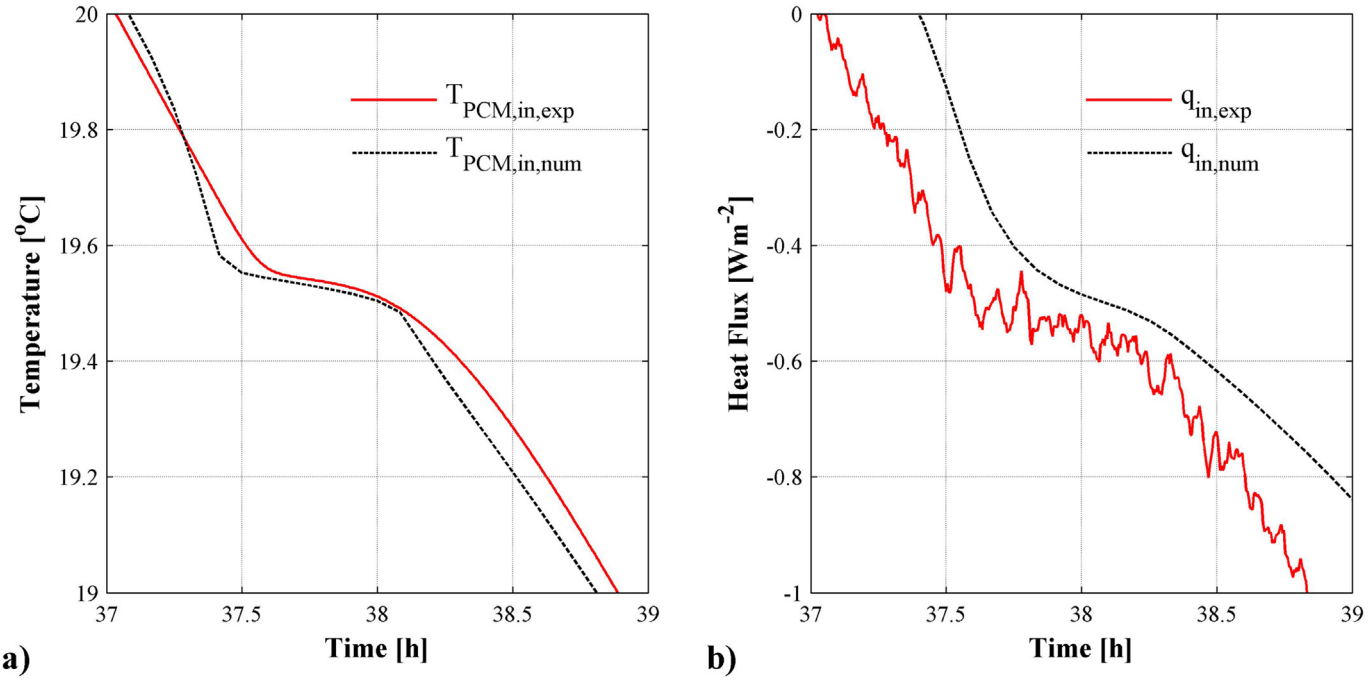

Fig. 12. Comparison of the experimental with the predicted values using the optimized artificial C_{eff} curves. (a) Detailed view of Fig. 11a and (b) Detailed view of Fig. 11d.

signal cannot capture the difference between the heat capacity of the PCM in the solid and liquid state.

The observations regarding the deviations in temperature results are clearly reflected in the heat flux curves at the respective measuring locations (Fig. 13c and d). The differences of the minimum temperatures correspond to the differences of the experimental and numerical heat fluxes during the same period of time. An additional observation concerns the deviation in the maximum heat flux values at the exposed surface of the SS –PCM (Fig. 13c). A closer look at the temperature diagram at the same location (Fig. 13a) reveals a small temperature difference at approximately 22.5 °C. This is most likely associated with the second peak near 22 °C in the heating DSC C_{eff} curve that was not taken into account in the artificial curve.

4. Conclusions

The new methodology put forward in this study proposes an alternative way for the determination of the effective heat capacity curves, for use in numerical modeling of phase change materials. From the standpoint of this paper, up to date existing practices suffer from their inability to deal with the PCM enhanced building component in its final (ready to use) form. Therefore, a hybrid methodology is proposed combining diverse experimental and numerical tools. It takes advantage of the latest advances in the dynamic testing of PCM enhanced building components, the dynamic operated heat flow meter apparatus, to perform dynamic measurements of PCM enhanced building panels. In the proposed methodology, experimental results of the thermal response of PCM enhanced panels are compared with predictions of a numerical model employing the effective heat capacity method in an optimization algorithm in order to provide optimum artificial effective heat capacity curves for the melting and crystallization processes of the PCM.

The methodology was applied for the determination of the effective heat capacity (C_{eff}) of a shape stabilized PCM attached on an insulation panel to form a lightweight building component combining the advantages of high thermal resistance with increased thermal mass. The thermal response of the building component was measured by a dynamic operated heat flow meter apparatus (DHFMA), providing different boundary conditions in two test cases. The first test case was used in order to define and optimize the artificial C_{eff} curves, while the second was used in order to validate the results.

Simulations of the first test case using the estimated artificial C_{eff} curves were proven to outperform the respective simulations using the curves defined by the DSC measurements with the use of the same numerical model. The artificial curves were proven superior in capturing the heat flux and temperature response of the building component associated with intense solidification and subcooling phenomena. Besides, the limitations of the DSC analysis, especially in the case of the determination of the cooling C_{eff} curves, were revealed. The cooling peak temperature of the studied PCM was a strong function of the heating rate and even at the low heating rates (1 °C min^{-1} and 0.1 °C min^{-1}), it did not appear to stabilize. The DHFMA measurements showed a different cooling behavior with a peak approximately 2.5 °C higher than the respective DSC peak at 0.1 °C min^{-1}.

Moreover, simulations of the second test case using the C_{eff} curves obtained with the hybrid methodology confirmed the findings and proved that the curves are not case dependent and can be successfully applied for simulation of the building component under similar temperature and heat flux conditions. Finally, the artificial curves revealed the real nature of phase change process in the final form of the PCM enhanced element in conditions similar to the real application.

It should be noted that the proposed methodology is not limited to a particular temperature range. With the use of a high temperature DHFMA, it could be applied for the determination of the C_{eff} associated with high temperature dehydration reactions [42] and [43] of building panels under fire conditions.

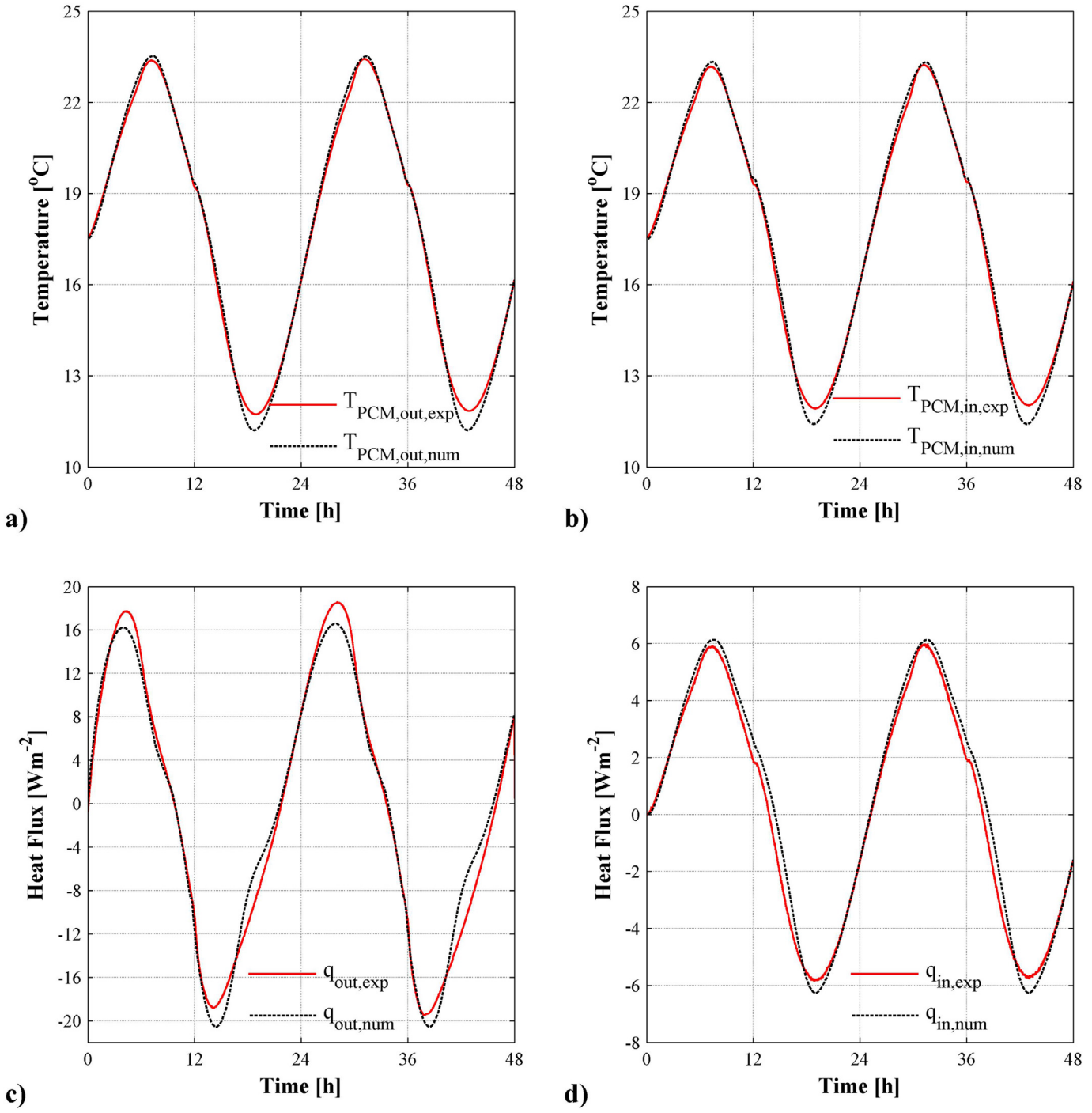

Fig. 13. Comparisons of the numerical simulation results using the optimized artificial C_{eff} curves with the DHFMA measurements of test case 2 showing (a) temperature at the exposed side of the SS – PCM, (b) temperature at the interface of SS – PCM and EPS, (c) heat flux at the heating/cooling plate simulating outdoor conditions and (d) heat flux at the heating/cooling plate simulating indoor constant temperature.

Acknowledgments

The authors acknowledge the financial support of the Fire-Facts project within the frame of ARISTEIA action (operational program 'Education and Lifelong Learning') that is co-financed by Greece and the European Union.

References

[1] Castellón C, Medrano M, Roca J, Cabeza LF, Navarro ME, Fernández AI, et al. Effect of microencapsulated phase change material in sandwich panels. Renew Energy October 2010;35(10):2370–4.

[2] Mandilaras I, Stamatiadou M, Katsourinis D, Zannis G, Founti M. Experimental thermal characterization of a Mediterranean residential building with PCM gypsum board walls. Build Environ March 2013;61:93–103.

[3] Dutil Y, Rousse DR, Salah NB, Lassue S, Zalewski L. A review on phase-change materials: mathematical modeling and simulations. Renew Sustain Energy Rev 2011;15:112–30.
[4] Yang H, He Y. Solving heat transfer problems with phase change via smoothed effective heat capacity and element-free Galerkin methods. Int Commun Heat Mass Transf April 2010;37(4):385–92.
[5] Dutil Y, Rousse D, Lassue S, Zalewski L, Joulin A, Virgone J, et al. Modeling phase change materials behavior in building applications: comments on material characterization and model validation. Renew Energy January 2014;61:132–5.
[6] Foong CW, Nydal OJ, Løvseth J. Investigation of a small scale double-reflector solar concentrating system with high temperature heat storage. Appl Therm Eng July 2011;31(10):1807–15.
[7] Egolf PW, Manz H. Theory and modeling of phase change materials with and without mushy regions. Int J Heat Mass Transf December 1994;37(18): 2917–24.
[8] Chiu JNW, Martin V. Submerged finned heat exchanger latent heat storage design and its experimental verification. Appl Energy May 2012;93: 507–16.
[9] Diarce G, Campos-Celador Á, Martin K, Urresti A, García-Romero A, Sala JM. A comparative study of the CFD modeling of a ventilated active façade including phase change materials. Appl Energy August 2014;126: 307–17.
[10] Ali Memon S. Phase change materials integrated in building walls: a state of the art review. Renew Sustain Energy Rev March 2014;31:870–906.
[11] Günther E, Hiebler S, Mehling H, Redlich R. Enthalpy of phase change materials as a function of temperature: required accuracy and suitable measurement methods. Int J Thermophys 2009;30:1257–69.
[12] Lazaro A, Peñalosa C, Solé A, Diarce G, Haussmann T, Fois M, et al. Intercomparative tests on phase change materials characterisation with differential scanning calorimeter. Appl Energy September 2013;109:415–20.
[13] Hunger M, Entrop AG, Mandilaras I, Brouwers HJH, Founti M. The behavior of self-compacting concrete containing micro-encapsulated phase change materials. Cem Concr Compos November 2009;31(10):731–43.
[14] Yinping Z, Yi J. A simple method, the-history method, of determining the heat of fusion, specific heat and thermal conductivity of phase-change materials. Meas Sci Technol 1999;10:201–5.
[15] Kravvaritis ED, Antonopoulos KA, Tzivanidis C. Improvements to the measurement of the thermal properties of phase change materials. Meas Sci Technol 2010;21 [art. no. 045103].
[16] Kosny J, Kossecka E, Brzezinski A, Tleoubaev A, Yarbrough D. Dynamic thermal performance analysis of fiber insulations containing bio-based phase change materials (PCMs). Energy Build September 2012;52:122–31.
[17] Pomianowski M, Heiselberg P, Lund Jensen R, Cheng R, Zhang Y. A new experimental method to determine specific heat capacity of inhomogeneous concrete material with incorporated microencapsulated-PCM. Cem Concr Res January 2014;55:22–34.
[18] Urresti A, Sala JM, García-Romero A, Diarce G, Escudero C. Validation of heat transfer models for PCMs with a conductivimeter. Energy Procedia 2012;30: 395–403.
[19] Kontogeorgos D, Founti M. Numerical investigation of simultaneous heat and mass transfer mechanisms occurring in a gypsum board exposed to fire conditions. Appl Therm Eng August 2010;30(11–12):1461–9.
[20] Barreneche C, Solé A, Miró L, Martorell I, Inés Fernández A, Cabeza LF. Study on differential scanning calorimetry analysis with two operation modes and organic and inorganic phase change material (PCM). Thermochim Acta 10 February 2013;553:23–6.
[21] Höhne GWH, Hemminger WF, Flammersheim HJ. Applications of differential scanning calorimetry. In: Differential scanning calorimetry. Springer; 2003. p. 147–244.
[22] ISO 8301:1991. Thermal insulation – determination of steady-state thermal resistance and related properties – heat flow meter apparatus. 1991.
[23] ASTM C518 – 10. Standard test method for steady-state thermal transmission properties by means of the heat flow meter apparatus. 2010.
[24] ASTM C1784 – 13. Standard test method for using a heat flow meter apparatus for measuring thermal storage properties of phase change materials and products. 2013.
[25] Kontogeorgos D, Ghazi Wakili K, Hugi E, Founti M. Heat and moisture transfer through a steel stud gypsum board assembly exposed to fire. Constr Build Mater January 2012;26(1):746–54.
[26] Mandilaras I, Kontogeorgos D, Founti M. Implementation of the heat capacity method for modelling the thermal performance of Agglomerate Stones containing PCM. In: 9th IIR conference on phase-change materials and slurries for refrigeration and air conditioning; October 2010 [Bulgaria, Sofia].
[27] Minkowycz W, Sparrow EM. Advances in numerical heat transfer (vol. 1), chapter 9. In: Voller VR, editor. An overview of numerical methods for solving phase change problems; 1997. p. 347–8.
[28] Rangaiah GP, Bonilla-Petriciolet A. Multi-objective optimization in chemical engineering: developments and applications, chapter 13. In: Tarafder A, editor. Modeling and multi-objective optimization of a chromatographic system. Wiley; 2013.
[29] Gear CW. Automatic integration of ordinary differential equations. Commun ACM 1971;14:176–9.
[30] Boersma SL. A theory of differential thermal analysis and new methods of measurement and interpretation. J Am Ceram Soc 1955;38(8):281–4.
[31] Castellón C, Günther E, Mehling H, Hiebler S, Cabeza LF. Determination of the enthalpy of PCM as a function of temperature using a heat-flux DSC–a study of different measurement procedures and their accuracy. Int J Energy Res 2008;32:1258–65.
[32] ISO 11357–4:2005. Plastics – differential scanning calorimetry (DSC) – part 4: determination of specific heat capacity. 2005.
[33] ASTM E1269 – 11. Standard test method for determining specific heat capacity by differential scanning calorimetry. 2011.
[34] ASTM E793-06. Standard test method for enthalpies of fusion and crystallization by differential scanning calorimetry. 2006.
[35] ISO 11357–3:2011. Plastics – differential scanning calorimetry (DSC) – part 3: determination of temperature and enthalpy of melting and crystallization. 2011.
[36] Arkar C, Medved S. Influence of accuracy of thermal property data of a phase change material on the result of a numerical model of a packed bed latent heat storage with spheres. Thermochim Acta November 2005;438(1–2): 192–201.
[37] He B, Martin V, Setterwall F. Phase transition temperature ranges and storage density of paraffin wax phase change materials. Energy September 2004;29(11):1785–804.
[38] Alkan C, Sarı A, Karaipekli A, Uzun O. Preparation, characterization, and thermal properties of microencapsulated phase change material for thermal energy storage. Sol Energy Mater Sol Cells 2009;93:143–7.
[39] Solomon GR, Velraj R. Analysis of the heat transfer mechanisms during energy storage in a phase change material filled vertical finned cylindrical unit for free cooling application. Energy Convers Manag November 2013;75:466–73.
[40] Solomon GR, Karthikeyan S, Velraj R. Sub cooling of PCM due to various effects during solidification in a vertical concentric tube thermal storage unit. Appl Therm Eng 15 April 2013;52(2):505–11.
[41] Emmel MG, Abadie MO, Mendes N. New external convective heat transfer coefficient correlations for isolated low-rise buildings. Energy Build 2007;39(3):335–42.
[42] Kontogeorgos D, Mandilaras I, Founti M. Scrutinizing gypsum board thermal performance at dehydration temperatures. J Fire Sci 2011;29:111–30.
[43] Kontogeorgos DA, Mandilaras ID, Founti MA. Fire behavior of regular and latent heat storage gypsum boards. Fire Mater 2015. http://dx.doi.org/10.1002/fam.2246.